SPIN-ORBIT TORQUE BASED HETEROSTRUCTURES FOR MRAM APPLICATIONS AND NEUROMORPHIC COMPUTING

DURGESH KUMAR OJHA

DEPARTMENT OF PHYSICS
INDIAN INSTITUTE OF TECHNOLOGY DELHI
NOVEMBER 2024

© Indian Institute of Technology Delhi (IITD), New Delhi, 2024

Spin-Orbit Torque Based Heterostructures for MRAM Applications and Neuromorphic Computing

by

DURGESH KUMAR OJHA

DEPARTMENT OF PHYSICS

Submitted

in fulfillment of the requirements of the Degree of Doctor of Philosophy

to the

INDIAN INSTITUTE OF TECHNOLOGY DELHI

November 2024

Dedication

- This Thesis is dedicated to the memory of my late father, **Sri Markanday Ojha,** who inspired me greatly to pursue this highest academic degree. He passed away in July 2020 and did not live to see this achievement.

- This Thesis is also dedicated to my dearest mother, **Ms. Madhuri Devi,** who encouraged and supported me during my challenging times.

DECLARATION

I certify that

a. The work contained in this thesis is original and has been done by me under the guidance of my supervisors;
b. For the award of a joint Degree, the results contained in this thesis have been submitted to National Yang Ming Chiao Tung University, Taiwan, under a Joint Degree program between IIT-D and NYCU-Taiwan;
c. I have followed the guidelines provided by the institution while preparing my thesis;
d. I have conformed to the ethical norms and guidelines while writing this thesis;
e. Whenever I have incorporated materials such as data, models, figures, and text from external sources, I have diligently acknowledged their contributions by citing them appropriately within the thesis text and providing comprehensive details about these sources in the references section.

Durgesh Kumar Ojha

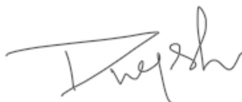

CERTIFICATE

This is to certify that the thesis entitled **"Spin-Orbit Torque-based Heterostructures for MRAM Applications and Neuromorphic Computing"** submitted by Mr. Durgesh Kumar Ojha, to the Indian Institute of Technology Delhi for the award of the Degree of **"DOCTOR OF PHILOSOPHY"** is a record of bonafide research work carried out by him under our guidance and supervision.

In our assessment, this thesis meets the criteria outlined by all relevant regulations pertaining to the degree requirements. For the award of a Joint Degree, the results contained in this thesis have also been submitted to National Yang Ming Chiao Tung University (NYCU) Taiwan, as a part of the IITD-NYCU Joint Degree Programme.

Supervisor 1.

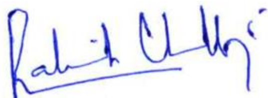

Prof. Ratnamala Chatterjee

Department of Physics

Indian Institute of Technology

New Delhi-110016, India

Supervisor 2.

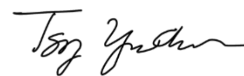

Prof. Yuan-Chieh Tseng

Department of Material Science and Engineering

National Yang Ming Chiao Tung University

Hsin-Chu, Taiwan 30010, ROC

Acknowledgments

It is with immense pleasure that I extend my heartfelt gratitude to everyone who contributed to this thesis. I wish to convey my profound gratitude to my advisors, Prof. Ratnamala Chatterjee and Prof. Yuan-Chieh Tseng, for their visionary guidance, unwavering support, and enthusiasm. Their encouragement, patience, and timely guidance expanded my perspectives and enriched my knowledge. Their time and assistance, both technically and non-technically, were invaluable, especially in crafting journal manuscripts and shaping this thesis, laying the foundation for a successful research career.
I would like to acknowledge my Doctoral committee members Prof. Santanu Ghosh, Prof. P.K. Muduli, and Prof. Debanjam Bhowmik for their valuable suggestions during the evolution of this research work. Further, I extend my sincere thanks to the Joint Degree Programme team of the IIT Delhi and NYCU-Taiwan for providing me with an opportunity to do research in the epicenter of semiconductor technology in Taiwan.

I would like to thank the National Synchrotron Radiation Research Centre Taiwan, Nano Facility Centre NYCU Taiwan, and Nano Research Facility of IIT-Delhi for providing world-class fabrication and characterization facilities. I am thankful to the Department of Science and Technology for giving me an award of INSPIRE FELLOWSHIPS, and to the Ministry of Human Resource Development, India for funding the research.

I thank all my seniors and lab members at IITD, including Dr. Vishal Bhardwaj, Dr. Anupam Bhattacharya, Dr. Priyanka Sharma, Dr. Hitesh Gulati, Dr. Divya Prakash Dubey, Shivangi Srivastava, Vikash Chahar, and Balawant Chauhan, for their cooperation and support. I would also like to thank my NYCU lab members in Taiwan, including Dr. Chih-Wei Cheng, Yu-Han Huang, Yu-Lon Lin, Yu-Hui Wu, Yu-Hsin Huang, and Ju Hsu, for their cooperation and support. Without their help, this thesis would not have been possible. A special thanks to Dr. Deepali for her unwavering moral support and cooperation throughout my Ph.D. journey.

Words cannot fully express my gratitude for the unconditional support of my family, who stood by me through every challenge. My heartfelt thanks go to my mother, Ms. Madhuri Devi and sisters, Mrs. Sony Ojha and Mrs. Shalini Ojha, for their constant encouragement. I am also

thankful to my brother-in-law, Mr. Manish Dubey and Mr. Neetish Pandey, for their support and cooperation.

A special mention goes to my uncle, Mr. Subash Prasad Tripathi, whose blessings and support were invaluable during my toughest times.

I am also deeply grateful to all my teachers and everyone who contributed to the completion of this thesis. Your guidance and support have been instrumental in this journey.

IIT-Delhi-India

27/11/2024

Durgesh Kumar Ojha

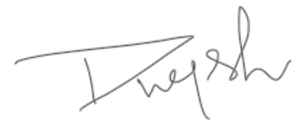

Abstract

The spin-orbit torque (SOT) generated by materials with significant spin-orbit coupling offers a promising avenue for developing energy-efficient and fast SOT-based memory and neuromorphic computing (NC) devices. SOT magnetization switching in ferromagnets (FM) with large perpendicular magnetic anisotropy (PMA) is particularly promising for next-generation non-volatile magnetoresistive random access memory (MRAM). This technology requires a high-performance pure spin current source with a large spin Hall angle and high electrical conductivity, achievable through mass production techniques. While SOT-induced switching typically needs an external magnetic field to break symmetry, achieving field-free switching (FFS) in perpendicularly magnetized FM layers is crucial for advancing high-density memory technology.

In the first part of this thesis, we utilized a new class of quantum material as a spin-density generator source, specifically topological insulators (TIs) like Bi_2Se_3, CoFeB was used as the FM layer, with various thin insertion layers of Pt, Ta, and Cu placed between the Bi_2Se_3 and FM films. We developed these multilayer Bi_2Se_3/insertion-layers/CoFeB structures using magnetron sputtering at room temperature. The study examined how the intermixing chemical state and additional Co-Pt interface influence the damping-torque efficiency of these sputtered TI-based SOT devices. A significant enhancement in SOT efficiency was observed in Pt insertion-based SOT devices.

In the next part, we developed sputtered heterostructures of W/Pt/Co(FM)/NiO/Pt samples with varying NiO thicknesses. Grazing incidence wide-angle X-ray scattering measurement confirmed that thick NiO (30nm) exhibited robust antiferromagnetic (AFM) ordering. Current-induced perpendicular magnetization switching of the Co layer was observed under the SOT scheme. FFS under minimal current density was achieved in thick NiO cases due to the exchange bias effect.

In the last part, we examined the neuromorphic characteristics of NiO-based SOT devices for NC applications. We observed the memristive behavior and intermediate magnetization state of W/Pt/Co/NiO/Pt devices. Using the experimental results from these NiO-based SOT devices, we constructed artificial synapses and sigmoidal neurons. We then implemented an artificial neural network in Python, based on these synapses and neurons, achieving remarkable pattern recognition accuracy on the Modified National Institute of Standard and Technology (MNIST) dataset.

सारांश

स्पिन–ऑर्बिट कपलिंग वाले सामग्रियों द्वारा उत्पन्न स्पिन–ऑर्बिट टॉर्क (SOT) ऊर्जा–कुशल और तेज SOT-आधारित मेमोरी और न्यूरोमोर्फिक कंप्यूटिंग (NC) उपकरणों के विकास के लिए एक आशाजनक मार्ग प्रदान करता है। बड़ी पेरपेंडिकुलर मैग्नेटिक एनीसोट्रॉपी (PMA) वाले फेरोमैग्नेट्स (FM) में SOT मैग्नेटाइजेशन स्विचिंग अगली पीढ़ी की नॉन–वोलाटाइल मैग्नेटोरेसिस्टिव रैंडम एक्सेस मेमोरी (MRAM) के लिए विशेष रूप से आशाजनक है। इस तकनीक के लिए बड़े स्पिन हॉल एंगल और उच्च विद्युत चालकता वाले उच्च–प्रदर्शन शुद्ध स्पिन करंट स्रोत की आवश्यकता होती है, जिसे बड़े पैमाने पर उत्पादन तकनीकों के माध्यम से प्राप्त किया जा सकता है। जबकि SOT-प्रेरित स्विचिंग को आमतौर पर समरूपता तोड़ने के लिए एक बाहरी चुंबकीय क्षेत्र की आवश्यकता होती है, पेरपेंडिकुलरली मैग्नेटाइज्ड FM लेयरों में फील्ड–फ्री स्विचिंग (FFS) प्राप्त करना उच्च–घनत्व मेमोरी तकनीक को आगे बढ़ाने के लिए महत्वपूर्ण है।

इस शोध प्रबंध के पहले भाग में, हमने एक नई श्रेणी की क्वांटम सामग्री का उपयोग स्पिन–डेंसिटी जनरेटर स्रोत के रूप में किया, विशेष रूप से टोपोलॉजिकल इंसुलेटर्स (TIs) जैसे Bi_2Se_3। CoFeB को FM लेयर के रूप में इस्तेमाल किया गया, जिसमें विभिन्न पतली इंसर्शन लेयरें Pt, Ta, और Cu को Bi_2Se_3 और FM फिल्मों के बीच रखा गया। हमने इन बहुस्तरीय Bi_2Se_3/इंसर्शन–लेयर/CoFeB संरचनाओं को कमरे के तापमान पर मैग्नेट्रॉन स्पटरिंग का उपयोग करके विकसित किया। अध्ययन ने जांच की कि इन स्पटर TI-आधारित SOT उपकरणों की डैम्पिंग–टॉर्क दक्षता पर इंटरमिक्सिंग केमिकल स्टेट और अतिरिक्त Co-Pt इंटरफेस का क्या प्रभाव पड़ता है। Pt इंसर्शन–आधारित SOT उपकरणों में SOT दक्षता में महत्वपूर्ण वृद्धि देखी गई।

अगले भाग में, हमने W/Pt/Co(FM)/NiO/Pt नमूनों के स्पटर किए गए हेटरोस्ट्रक्चर्स को विकसित किया, जिनमें NiO की मोटाई विभिन्न थी। ग्रेज़िंग इन्सिडेंस वाइड–एंगल एक्स–रे स्कैटरिंग मापन ने पुष्टि की कि मोटे NiO (30nm) ने मजबूत एंटीफेरोमैग्नेटिक (AFM) क्रम दिखाया। SOT योजना के तहत Co लेयर की करंट–प्रेरित पेरपेंडिकुलर मैग्नेटाइजेशन स्विचिंग देखी गई। एक्सचेंज बायस प्रभाव के कारण मोटे NiO मामलों में न्यूनतम करंट घनत्व के तहत FFS प्राप्त हुआ।

अंतिम भाग में, हमने NC अनुप्रयोगों के लिए NiO-आधारित SOT उपकरणों की न्यूरोमोर्फिक विशेषताओं का परीक्षण किया। हमने W/Pt/Co/NiO/Pt उपकरणों का मेमरेसिव व्यवहार और

इंटरमीडिएट मैग्नेटाइजेशन स्टेट देखा। इन NiO-आधारित SOT उपकरणों से प्राप्त प्रायोगिक परिणामों का उपयोग करते हुए, हमने कृत्रिम सिनैप्स और सिग्मॉइडल न्यूरॉन्स का निर्माण किया। इसके बाद, हमने इन सिनैप्स और न्यूरॉन्स पर आधारित एक कृत्रिम न्यूरल नेटवर्क को Python में लागू किया, जिससे मॉडिफाइड नेशनल इंस्टीट्यूट ऑफ स्टैंडर्ड्स एंड टेक्नोलॉजी (MNIST) डेटासेट पर उल्लेखनीय पैटर्न पहचान सटीकता प्राप्त हुई।

Contents

Certificate i

Acknowledgments ii

Abstract iv

सारांश vi

Contents viii

List of Figures xii

List of Tables xxii

List of symbols and Abbreviation xxiv - xxviii

Chapter 1 Introduction 1

1.1 Basic Concept of Spintronic and an Overview of MRAM 1

1.2 Spin Torque Generation for Magnetization Switching 4

1.2.1 Spin Transfer Generation for Magnetization Switching 4

1.2.2 Spin-Orbit Torque (SOT) 5

1.2.3 Spin Hall Effect (SHE) 6

1.2.4 Interfacial Rashba Edelstein Effect (IREE) 8

1.3 Damping-Like Torque and Field-Like Torque 9

1.4 Materials for SOT MRAM 10

1.4.1 Spin Density Generators for SOT 10

1.4.2 Heavy Metals 10

1.4.3 Heavy Metals Alloys 11

1.4.4 Multilayers/Heterostructure 12

1.4.5 Self-Spin Orbit Torque 14

1.4.6 Ion Implantation and Doping 15

1.4.7 Topological Insulators 15

1.5 Why CoFeB is a Ferromagnetic Layer for Memory Applications 16

1.6 Spintronic-Based Magneto Resistive Random Access Memory 17

1.6.1 STT and SOT-based MRAM 17

1.7 Field-Free Switching for SOT-based Logic Devices 19
1.8 Neuromorphic Computing 20
1.8.1 Advancements in SOT-Based Devices for Neuromorphic Computing 21
1.8.2 Artificial Synapse(LTD/LTP) 22
1.8.3 Sigmoidal Neuron 23
1.9 Objective 24
1.10 Thesis Plan 27

Chapter 2 Experimental Method and Computational Analysis 30
2.1 Experimental Procedure and Characterization Techniques 30
2.1.1 Growth and Characterization of Bi_2Se_3/ (Pt, Ta, Cu)/CoFeB/Ta 32
2.1.2 Growth and Characterization of W/ Pt/Co/NiO/Pt 33
2.1.3 Neuromorphic Computing in W/ Pt/Co/NiO/Pt-based SOT System 33
2.2 Sample Preparation 33
2.2.1 Ultra-High Vacuum Sputtering System 33
2.2.2 Deposition Parameters of Heterostructures 36
2.3 Heterostructure Characterization Technique 38
2.3.1 Vibrating Sample Magnetometer 38
2.3.2 X-ray Magnetic Circular Dichroism 40
2.3.3 Angle-dependent X-ray Photoelectron Spectroscopy 42
2.3.4 Grazing Incidence Wide-angle X-ray Scattering 44
2.4 Device Fabrication Process 45
2.5 Electrical Transport Measurements 45
2.5.1 Planar Hall Measurements for SOT Efficiency 46
2.5.2 Electrical Measurements 48
2.6 Computational Technique for MNIST Pattern Recognition Task 49
2.6.1 Artificial Neural Network 49

2.6.2 MNIST and Fashion MNIST images 50

Chapter 3 Interface Engineering to Enhance Spin Torque Efficiency in Sputtered Bismuth Selenide 52

3.1 Introduction 52

3.2 Experimental Method 55

3.3 Results and Discussions 56

3.3.1 Structural Characterization 56

3.3.2 Orbital and Spin Magnetic Moment 57

3.3.3 Branching Ratio Calculation and AR-XPS 61

3.3.4 SOT Efficiency of BS/Pt/CFB System 67

3.3.5 SOT Efficiency of BS/Ta(0.5)/CFB System 74

3.4 Conclusion 76

Chapter 4 Current-Induced Field-Free Switching of NiO-based SOT Device Through Exchange Bias 77

4.1 Introduction 77

4.2 Experimental Section 78

4.2.1 Growth of Samples and Device Fabrication 78

4.2.2 Electrical and GIWAXS Measurements 79

4.3 Results and Discussion 79

4.3.1 Antiferromagnetic ordering from GIWAXS 79

4.3.2 Perpendicular Exchange Bias 83

4.3.3 Current-induced Out-of-plane effective field 84

4.3.4 Current-induced SOT switching loop 88

4.3.5 Switching Phase Diagram 91

4.3.6 Switching Percentage 92

4.3.7 Loop Shift Measurement 94

4.4 Conclusion 98

Chapter 5 Neuromorphic Computing with the Ferromagnetic/Antiferromagnetic NiO-based SOT System 99

5.1 Introduction 99

5.2 Experimental Sections 101

5.3 Results and Discussion 101

5.3.1 Memristive Behaviour and Intermediate Magnetization States 101

5.3.2 An artificial synapse in the context of LTD/LTP 104

5.3.3 A Sigmoidal Neuron 106

5.3.4 MNIST Pattern Recognition Task 109

5.3.5 Impact of Nonlinearity and Symmetric Characteristics 114

5.3.6 Three Digit/Character MNIST Accuracy 118

5.3.7 Fashion MNIST Images Recognition Task 120

5.4 Conclusion 123

Chapter 6 Summary of Thesis and Prospects for Future Research 124

6.1 Summary of Our Research Work 124

6.2 Prospects of Future Research for Neuromorphic Computing 126

6.2.1 Challenge in Scaling of Hall-bar Device 126

6.2.2 Enhancing Signal Output and Hall Resistance for Future Devices 126

6.2.3 Linear and Symmetric Weight Variation 127

6.2.4 Strategy for Further Energy Reduction 127

6.3 Conclusion 128

References 129

Appendix-A 150

List of Publications 162

Author Biography 163

List of Figures

Figure No:	Figure Title	Page No.
1.1	A schematic diagram of the current memory hierarchy	3
1.2	Spin Transfer Torque Effect in Magnetic Tunnel Junction	5
1.3	Writing current path illustration for Spin-Orbit Torque device in the SOT switching scheme.	6
1.4	A 3-D visualization of the Spin Hall Effect.	7
1.5	A-3D visualization of the Interfacial Rashba Effect.	8
1.6	A schematic of various materials sources for SOT-MRAM	10
1.7	A schematic diagram of SOT-based MRAM	18
1.8	A schematic of various methods to achieve field-free switching	20
1.9	Schematic diagram of my thesis work: SOT-based heterostructures for MRAM applications and neuromorphic computing	26
2.1	The schematic diagram depicts the experimental procedure and techniques used in this work. The top, middle, and bottom figures correspond to chapters 3, 4, and 5 respectively.	31
2.2	Schematic illustration of vibrating sample magnetometer assembly	39
2.3	M-H loop of Bi_2Se_3/CoFeB(t)/Ta system: the thickness of CoFeB layers varies from 1.8nm to 6.4nm as shown in the graph.	40
2.4	Schematic diagram of XMCD measurements and its working principle	41
2.5	Synchrotron measurements setup: sample mounting and its measurements at TLS09 Hsinchu NSRRC.	42
2.6	(a) Schematic presentation of XPS measurement set-up and (b) illustrates its working principles.	43

2.7	The schematic illustration of the scattering geometry of GIWAXS measurements	44
2.8	Hall-bar Device Fabrication Process (left) and the SEM, OM images of the fabricated Hall-bar device (right)	45
2.9	Hall bar device geometry under electrical transport measurement	46
2.10	Current Shunting Model: crossectional view of Bi_2Se_3/Pt/CFB heterostructure	47
2.11	Schematic of Electrical Transport Measurements: Probe station. This setup is fully automated and controlled by a LabVIEW Program.	48
2.12	The implemented ANN for MNIST image recognition accuracy consists of three layers with 784 input neurons, two hidden layers with 10 neurons each, and an output layer with 4 neurons. Each MNIST image character is 28×28 pixels in size.	50
2.13	MNIST and Fashion MNIST Datasets	51
3.1	(a) Se-3d and (b) Bi-4f Core Level XPS Spectra; (c) Resistivity versus thickness of Bi_2Se_3 film; and (d) Atomic Force Microscopic Image of Bi_2Se_3 (7nm) thin film sputter-grown on Si Substrate at room temperature.	57
3.2	XAS and XMCD spectra of Bi_2Se_3(7)/Pt/CoFeB (5) system. (a) and (b) present the Fe $L_{2,3}$ XAS and XMCD spectra. (c) and (d) depicted the Co $L_{2,3}$ XAS and XMCD spectra respectively	58
3.3	XAS, XMCD spectra of insertion-based samples utilized for sum rule analysis. (a),(b), and (c) illustrated Fe $L_{2,3}$ spectra of BS/Ta(0.5)/CFB,BS/Pt(0.5)/CFB and BS/Cu(0.5)/CFB respectively. (d)-(f) depicted the Co $L_{2,3}$ spectra of the same samples respectively. These p, q, and r values of each sample are utilized from their spectra to calculate their orbital and spin magnetic moment using sum rule analysis.	59
3.4	Orbital to spin magnetic moment ratio of all insertion-based samples. (a) illustrate each insertion-based sample. (b) and (c)	60

depicted the ratio of orbital and spin magnetic moment of each sample for Fe and Co atoms respectively.

3.5 (a)-(c) XAS and its integrated spectra (upper part of each fig.) and XMCD & its integrated spectra (lower part of each fig.) of BS/Pt/CFB, BS/Cu/CFB, and BS/Ta/CFB samples respectively. (d) illustrate the combined Co $L_{2,3}$ XAS, XMCD, and its respective integrated spectrum of all insertion-based samples. These integrated XAS are utilized to calculate the branching ratio of each sample. 62

3.6 Se-3*d* core level XPS spectra of IBH system., (a), (b) XPS spectra of BS/Pt (1.0nm)/CFB & BS/Pt (0.5nm)/CFB samples at an incident angle of 0°, 30° and 55° respectively. (c), (d) XPS spectra of BS/Ta (1.0nm)/CFB & BS/Cu (1.0nm)/CFB samples at incident angles of 0° and 55° respectively. 63

3.7 (a) and (b) show the core level AR-XPS of Pt-4*f* and Bi-4*f* recorded for BS(7nm)/Pt (0.5nm)/CFB(1.8nm) respectively 65

3.8 (a)The M-H loop of Bi_2Se_3(7)/Pt/CoFeB (5)/Ta (2) system under different Pt insertion layers, (b) Average saturation magnetization of Bi_2Se_3(7)/CoFeB (5)/Ta and Bi_2Se_3(7)/Pt/CoFeB (5)/Ta system versus the thickness of CoFeB layers; the magnetic dead layer of both systems are 1.13nm and 0.74 nm respectively 67

3.9 3D-Schematic diagram, angle-dependent Hall resistance measurements**.** (a) A 3D schematic diagram illustrates the SOT in Bi_2Se_3/Pt/CoFeB heterostructure. (b) Hall measurement set-up. (c) and (d) represent the R_H (I, α) of Bi_2Se_3/CoFeB and Bi_2Se_3/Pt(0.5)/CoFeB(5) samples at ± 5.0mA respectively 68

3.10 Angle-dependent Hall resistance measurements, and SOT Characterization**.** (a) and (b) illustrate the R_{DH} (I, α) variation of Bi_2Se_3/CoFeB and Bi_2Se_3/Pt (0.5)/CoFeB (5) samples at different input currents respectively. (c) and (d) represent the 70

variation of Hoop versus J_{BS} of both structures, respectively. The SOT efficiency of Bi_2Se_3/CoFeB and Bi_2Se_3/Pt (0.5)/CoFeB (5) samples were determined by their respective slope

3.11 (a) The R_H (I, α) of Bi_2Se_3(7)/Pt(1)/CoFeB(5) samples at ± 5.0mA. (b) R_{DH} (I, α) variation of Bi_2Se_3/Pt(1)/CoFeB(5) samples at different input currents (3.0mA to 6mA). (c)The variation of the out-of-plane effective field with current density. 72

3.12 Resistance versus magnetic field at 1 mA input current for (a) Bi_2Se_3(7)/CFB, (b) BS/Pt (0.5)/CFB, and (c) BS/Pt (1.0)/CFB respectively 73

3.13 The variation of the out-of-plane effective field with current density, (b) benchmark diagram[172] 73

3.14 SOT efficiency of Bi_2Se_3(7)/Ta (0.5)/CoFeB (5) system. (a) and (b) depicted the R_H (I, α) and R_{DH} (I, α) of Bi_2Se_3/Ta(0.5)/CoFeB samples at ± 5.0mA and at different input currents respectively. (c) represents the variation of Hoop versus J_{BS} of Bi_2Se_3(7)/Ta (0.5)/CoFeB structures. The SOT efficiency of Bi_2Se_3(7)/Ta (0.5)/CoFeB samples was determined by their slope. 74

4.1 Crystallographic analysis of NiO-based samples with various thicknesses of NiO layers: (a) illustration of NiO-based samples, (b), (c), and (d) represents the GIWAXS patterns of NiO-2nm, NiO-15nm, and NiO-30nm samples respectively. All three samples revealed textured Pt and NiO crystallographic planes of (111), (200), (220), and (311). NiO-2nm sample presented the Pt crystallographic plane characteristics, whereas NiO-15nm and NiO-30nm samples exhibited NiO planes. 80

4.2 The extracted 2-θ profile of each NiO-based sample from their GIWAXS pattern: (a), (b), and (c) illustrate the ARXRD spectra of NiO-2nm, NiO-15nm, and NiO-30nm samples respectively at different polar angle (Ψ = 0°, 29.5°, 35.3°, 54.7°) . (d) show the 82

combined ARXRD profile of NiO-2nm, 15nm, and 30nm at Ψ = 0°. The transformation from the q-space to the 2-θ profile was achieved using a wavelength of 1.5418 Å.

4.3 Schematic device structure and perpendicular exchange bias effect. (a) NiO-based device structure with spin configuration (left) and set-up for Hall bar electrical measurements (right). (b) Hall resistance response under variation of perpendicular magnetic field (H_z), highlighting the PMA nature and switching properties of the NiO structure. (c),(d), and (e) show the hysteresis loop of Nio-2nm, NiO-15nm, and NiO-30nm samples under H_z respectively 83

4.4 Anomalous Hall effect measurements at H_x = 0 Oe; (a),(b), and (c) represent the AHE loop of NiO-2nm, NiO-15nm, and NiO-30nm devices respectively, under different bias currents. These AHE loops are used to calculate H_z^{eff} field 85

4.5 Anomalous Hall effect measurements (a),(b), and (c) represent the in-plane AHE loop of NiO-2nm, NiO-15nm, and NiO-30nm devices respectively, under different bias currents 86

4.6 Current-induced out-of-plane effective field (H_z^{eff}) of NiO-based devices: (a),(b), and (c) depicted the variation of H_c^+, H_c^-, and H_z^{eff} field with bias current density (J_c) for the NiO-2nm,-15nm, and NiO-30nm devices, respectively. The blue and pink respectively indicate positive (H_c^+) and negative (H_c^-) switching fields while the light green indicates the average (H_z^{eff}) of the devices 88

4.7 Current-induced magnetization switching loop of NiO-based SOT device: (a), (b), and (c) respectively illustrate the current-induced SOT switching loop of NiO-2nm, NiO-15nm, and NiO-30nm devices with H_x varied from + 70 Oe to -70 Oe (bottom to top). The positive and negative H_x values, respectively, indicate 90

the clockwise and anticlockwise rotation of the switching loop. The purple denotes the switching loop under H_x = 0 Oe for each device. (d) The FFS loop of NiO-based devices: the pink color (bottom) represents an incomplete switching loop corresponding to NiO-2nm, while the deterministic switching loops shown in green (middle) and blue (top) represent NiO-15nm and NiO-30nm devices, respectively

4.8 Switching phase diagram of NiO-based SOT devices; (a) illustration of clockwise and anticlockwise rotation of magnetization switching of Co layer under J_c and H_x. (b), (c), and (d) represent the NiO-2nm, NiO-15nm, and NiO-30nm devices respectively. The blue and pink color balls represent up-to-down and down-to-up switching current variation under different H_x for each device respectively 91

4.9 Switching percentage of our NiO-based devices; (a), (b), and (c) illustrate the switching percentage of NiO-2nm, NiO-15nm, and NiO-30nm devices respectively. (d) illustrate the switching ratio (%) of NiO2nm, NiO15nm, and NiO30nm samples under the in-plane field. The pink, green, and blue colors represent the NiO2nm, NiO15nm, and NiO30nm respectively 93

4.10 Loop shift results of NiO-based SOT device under H_x = ± 3kOe and bias current of ± 12 mA. (a), (c), and (e) show the AHE loop shift at H_x = 3kOe, (b), (d), and (f) illustrate the AHE loop of NiO2nm, NiO15nm, and NiO30nm device respectively at Hx = -3kOe. The blue and pink colour corresponds to +12mA and -12mA bias currents respectively 96

4.11 The variation of out-of-plane effective field (H_z^{eff}) with bias current (I_{dc}) under H_x = ± 3kOe. (a),(b), and (c) represent the H_z^{eff} response with bias current for NiO2nm, NiO15nm, and 97

NiO30nm devices respectively. (d) illustrate the H_z^{eff}/I_{dc} response under H_x.

5.1 SOT-based NiO samples and their current-induced switching loop. (a) schematic diagram of sample structure (left), with Hall-bar electrical measurement setup. (b) SEM image of Hall-bar device. (c) illustrates the current-induced switching loop of NiO-2nm(pink), NiO-15nm(green), and NiO-30nm (blue) at H_x= -300 Oe respectively. This switching loop indicates multiple intermediate R_{Hall} states 102

5.2 Memristive behavior and intermediate magnetization states in terms of R_{Hall} of our NiO-based SOT devices. (a), (c), and (e) illustrate the memristive characteristics of NiO-2nm, NiO-15nm, and NiO-30nm hall bar devices, respectively, under H_x = -300Oe. Different pulse current amplitudes (20 mA to 45 mA for NiO-2nm, 40 mA to 54 mA for NiO-15nm, and 29 mA to 45 mA for NiO-30nm) indicate the maximum pulse current amplitude during the switching loop. Figures (b), (d), and (f) depict the stable intermediate magnetization states of these devices in terms of R_{Hall}. The blue line represents the reset states and pink, violet, magenta & orange correspond to different R_{Hall} states at a particular current for each device respectively 103

5.3 LTD/LTP characteristics of our NiO-based SOT devices under applied pulse current: (a) schematic of biological neurons and synaptic connections; (b) schematic of fabricated Hall bar device under the setup of electrical measurements; (c) tuning of R_{Hall} using a sequence of 25 positive current pulses (blue and dark blue lines) with an amplitude of +40 mA (NiO-15nm) and +30 mA (NiO-2nm and NiO-30nm) and a pulse duration of 500 μs, followed by a corresponding set of 25 negative pulses (red and pink lines) with an amplitude of -40 mA (NiO-15nm) and -30 mA (NiO-2nm and NiO-30nm) and a pulse duration of 500 μs. 105

	(d), (e) and (f) present the 250 R_{Hall} response with pulse number (LTD and LTP response) under H_x = -300 Oe, for samples NiO-2nm, NiO-15nm, and NiO-30nm respectively.	
5.4	Sigmoidal artificial neuron (a) Normalized switching loop observed in NiO-based devices under H_x = -300 Oe. The pink, green, and blue circles, respectively, indicate the switching loop of samples NiO-2nm, NiO-15nm, and NiO-30nm. The activation function for an artificial neuron in the hidden layer is derived using the sigmoid function from the R_{Hall} data points in the shaded region. (b) The optimal R_{Hall} data points for NiO-2nm, NiO-15nm, and NiO-30nm devices were extracted from the shaded region of switching loop measurements as shown in Fig.5.4(a). These points were used to construct sigmoid functions represented by pink (NiO-2nm), green (NiO-15nm), and blue (NiO-30nm) circles, with their corresponding sigmoid fits depicted by lines of the same colors	107
5.5	Sigmoidal activation function derived from experimental SOT switching loop. (a) The sigmoid activation function of NiO2nm device. The pink circle represents the R_{Hall} intermediate multistate of the NiO-2nm SOT switching loop as shown in Figure 5.4(a). The pink line shows the fitted sigmoid function, and the inset box illustrates the fitted parameters, which were used in our Python code for NiO2nm neuromorphic recognition performance. (b), (c), and (d) represent the exp. R_{Hall} data point with respective fitted sigmoid functions of NiO2nm, NiO15nm, and NiO30nm respectively under repeated SOT switching loop. The different circles of each NiO-based device represent the repeated intermediate magnetization states (Exp. Data) in terms of the R_{Hall} of each device.	108
5.6	Artificial neural network for MNIST digits recognition accuracies. (a) ANN consists of 784 input layers, and 2 hidden	111

layers each consists 10 neurons and the output layer consists of 5 neurons. (b) and (d) depict test accuracies of MNIST digits: “1”, “2”, “4”, “6” and “0”, “2”, “3”, “6”, “9” respectively. (c) and (e) show corresponding training accuracies. The ANN utilized 150 R_{Hall} states of each NiO-based device as an artificial synapse, with their respective fitted sigmoid activation function. Orange color indicates the ideal case, while pink, green, and blue represent the exp. case results.

5.7 Artificial neural network for MNIST characters recognition accuracies. (a) ANN consists of 784 input layers, and 2 hidden layers each consisting of 10 neurons, and the output layer consists of 4 neurons. (b) and (d) depict test accuracies of MNIST characters: “NYCU” and “DKYC” respectively. (c) and (e) show corresponding training accuracies. Purple colour indicates the ideal case, while pink, green, and blue depict the exp. case results for NiO2nm, NiO15nm, and NiO30nm devices. 113

5.8 Nonlinearity analysis of NiO-based devices (a), (c), and (e), demonstrate the normalized LTD and LTP behavior of NiO-2nm, NiO-15nm, and NiO-30nm devices respectively. (b), (d), and (f) correspond to the nonlinearity analysis of NiO2nm,15nm, and NiO30nm devices under normalized conductance versus pulse number respectively. 116

5.9 (a) MNIST digits and (b) MNIST characters recognition accuracy of our NiO-based neuromorphic devices under case 1 and case 2 respectively. The pink, green, and blue colors illustrate the recognition accuracy of the NiO-2nm,15nm, and 30nm devices respectively. 117

5.10 ANN for three MNIST Digits and characters recognition accuracy. (a) ANN consists of a 3-layer, input layer consisting of 784 neurons, (b) and (d) illustrate the MNIST digits and characters recognition accuracy of our NiO-based SOT devices 119

respectively. (c) and (e) present the corresponding training accuracy of the devices. The purple circle represents the ideal case, while the pink, green, and blue colors correspond to the exp. case of NiO-2nm,15nm, and 30nm respectively

5.11 R_{Hall} vs pulse number (LTD/LTP) response of NiO-based SOT device. (a), (b), and (c) illustrates the 300 R_{Hall} response of NiO2nm, NiO15nm, and NiO30nm respectively. This 300 R_{Hall} vs pulse number experimental data was utilized as an artificial synapse for the Fashion MNIST pattern recognition task 120

5.12 Artificial Neural Network for Fashion MNIST pattern recognition accuracy. (a) ANN consists of the input layer, two hidden layers, and an output layer. (b), and (c) shows the test and train accuracy of NiO-based SOT devices respectively. Pink color represents the ideal case while red, green, and blue correspond to NiO2nm, NiO15nm, and NiO30nm exp. case respectively 121

List of Tables

Table No:	Title of the Table	Page No:
1.1	An overview of the SOT efficiency in heterostructures featuring HMs	11
1.2	An overview of the SOT efficiency in heterostructures featuring heavy metal alloys	12
1.3	An overview of the SOT efficiency in multilayers/heterostructures	13
1.4	An overview of the SOT efficiency in self-SOT materials	14
1.5	An overview of the SOT efficiency in ion implantation and doping materials	15
2.1	Deposition parameters of different insertion-based TIs heterostructure thin films	36
2.2	Insertion-based TIs heterostructure thin films	37
2.3	Deposition parameters of different NiO-based SOT heterostructure thin films.	38
3.1	AR-XPS fitting results: atomic percentage of intermixing chemical states of BS/Pt(0.5nm)/CFB systems, for Se-3*d*, Bi-4*f*, and Pt-4*f* core level, and Se-3*d* for BS/Pt (1)/CFB system.	66
3.2	Spin Hall angle (SOT efficiency) and electrical resistivity of several spin density generators/FM systems	75
4.1	The approximate critical switching current range of our NiO-based SOT device under different in-plane bias fields H_x = + 3kOe to -3kOe	92
4.2	The approximate switching percentage ratio of our NiO-based SOT device under H_x = 0 Oe, ±50 Oe, and ±500 Oe	94

5.1	MNIST images pattern recognition train and test accuracy of NiO-based SOT devices under ideal synapse and neurons (ideal case) and experimental synapse (R_{Hall} vs pulse number) and sigmoidal neurons (exp. case).	112
5.2	MNIST images pattern recognition test accuracy of NiO-based SOT devices under case1 (exp. sigmoidal neuron and ideal synapse) and case2 (ideal sigmoid neuron and exp. constructed synaptic weight)	117
5.3	The benchmark table includes MNIST/Fashion MNIST image pattern recognition accuracy, and types of experimental synaptic weight, used in artificial neural networks across various SOT-based devices	122

List of Symbols and Abbreviation

Symbols

θ_{SH}	Spin Hall Angle
M_s	Saturation Magnetization
J_c	Switching Current Density
t_{FM}	Thickness of the FM layer
$\hbar$	Reduced Plank Constant
H_x	In-plane external magnetic field
σ	Electrical Conductivity
BS	Bi_2Se_3
CFB	Co_{20} Fe_{60} B_{20}
m_{orb}	Orbital Magnetic Moment
m_{Spin}	Spin Magnetic Moment
p	Integrated XMCD spectra of L_3 peak
q	Integrated XMCD spectra of L_3+L_2
r	XAS Integral Value
eV	electron Volt
R_H	Angle-dependent Hall Resistance
R_{DH}	Difference of R_H
I	Input current
α	The angle between I and H_x
H_{OOP}	OOP effective magnetic field
R_{AHE}	Anomalous Hall Resistance
R_{PHE}	Planar Hall Resistance
ρ	Resistivity
ξ	SOT efficiency
ξ_{DL}	Damping-Like SOT efficiency
H_{EB}	Exchange Bias
R_{Hall}	Hall Resistance
H_z	Perpendicular Magnetic Field
H_z^{eff}	Current-induced OOP effective field
H_c	Coercive Field

$J_{av.swi}$	Average of Switching Current Density
ΔR_{SOT}	Change in R_{Hall} under SOT switching loop measurement
ΔR_{AHE}	Change in R_{Hall} during AHE measurement
μ_0	Vacuum Permeability
t_{spacer}	Thickness of Spacer Layer

List of Symbols and Abbreviation

Abbreviations

SOT	Spin-Orbit Torque
MRAM	Magneto-Resistive Random Access Memory
STT	Spin-Transfer Torque
SDG	Spin Density Generator
GMR	Giant Magneto-Resistance
TMR	Tunneling Magneto-Resistance
SRAM	Static Random Access Memory
DRAM	Dynamic Random Access Memory
HDD	Hard Disk Drive
MTJ	Magnetic Tunnel Junction
PMA	Perpendicular Magnetic Anisotropy
SHE	Spin Hall Effect
IREE	Interfacial Rashba Edelstein Effect
SOC	Spin-Orbit Coupling
FM	Ferromagnet
NM	Non-Magnet
HM	Heavy Metal
ST-FMR	Spin-Torque Ferromagnetic Resonance
SHA	Spin Hall Angle

TI	Topological Insulator
FFS	Field Free Switching
DMI	Dzyaloshinskii-Moriya interaction
OOP	Out-of-Plane
AFM	Antiferromagnetic
EB	Exchange Bias
AI	Artificial Intelligence
NC	Neuromorphic Computing
ANN	Artificial Neural Network
AR-XPS	Angle-resolved X-ray Photoelectron Spectroscopy
XMCD	X-ray Magnetic Circular Dichroism
XAS	X-ray Absorption Spectroscopy
GIWAXS	Grazing Incidence Wide Angle X-ray Scattering
SPD	Switching Phase Diagram
MNIST	Modified National Institute Standards Technology
IBH	Insertion Based Heterostructure
VSM	Vibrating Sample Magnetometer
XPS	X-ray Photoelectron Spectroscopy
AHE	Anomalous Hall Effect
LTD	Long Term Depression
LTP	Long Term Potentiation
MBE	Molecular Beam Epitaxy

IP	In-Plane
ISOC	Interfacial Spin-Orbit Coupling
RT	Room Temperature
SOS	Spin-Orbit Splitting
RF	Radio Frequency
BR	Branching Ratio
SOI	Spin-Orbit Interaction
MDL	Magnetic Dead Layer
AR-XRD	Angle-resolved X-ray Diffraction
SP	Spin-Polarized
UHV	Ultra High Vacuum
ANN	Artificial Neural Network
MLP	Multilayer Perceptron